Electronic Supplementary Material (ESI) for Nanoscale Horizons.

Supplementary Information

Single molecule localization-based analysis of clathrin-coated pit and caveolar dynamics

Rui Ma, [‡,a] Martin Štefl [‡,a] and Gerd Ulrich Nienhaus [a,b,c,d,*]

[a] Institute of Applied Physics (APH), Karlsruhe Institute of Technology (KIT), Wolfgang Gaede-Strasse 1, 76131 Karlsruhe, Germany.

[b] Institute of Nanotechnology (INT), Karlsruhe Institute of Technology (KIT), PO Box 3640, 76021 Karlsruhe, Germany.

[c] Institute of Biological and Chemical Systems (IBCS), Karlsruhe Institute of Technology (KIT), PO Box 3640, 76021 Karlsruhe, Germany.

[d] Department of Physics, University of Illinois at Urbana−Champaign, Urbana, IL 61801, USA.

[‡] These authors contributed equally: Rui Ma, Martin Štefl.
*email: uli@uiuc.edu

Contents

1. Supplementary Methods

Glass slide treatment. Microscope coverslips (diameter 24 mm, No. 1.5H, Marienfeld) were first pre-cleaned in a plasma cleaner for 1 h. Next, coverslips were incubated in 2% Hellmanex™ III (Hellma) at 65 °C overnight and washed six times with MilliQ water. Gold nanoparticles served as fiducial markers for drift correction when imaging fixed samples. Before growing cells, pre-cleaned coverslips were incubated for 20 min with 80 nm gold nanoparticle solution (BBI) 100-fold diluted in MilliQ water. Then, the coverslips were washed twice with MilliQ water.

Plasmid construction Mouse proteins (Cav3 and CLCa) were tagged with fluorescence proteins using NEBuilder HiFi DNA Assembly Cloning Kit (NEB). Zebrafish proteins (Cav3) were tagged using Gateway Recombination Cloning Technology (ThermoFisher Scientific).

Mouse myoblast cell culture. Mouse C3H muscle myoblasts (C2C12) were cultured in high glucose DMEM medium (11965092, ThermoFisher Scientific) containing 10% of fetal bovine serum (FBS, 10270106, ThermoFisher Scientific). The cells were adhered on pre-cleaned round coverslips in 6-well plates (M9062-100EA, Sigma-Aldrich). After reaching 50% confluency, the cells were transfected with 3 µg of a plasmid encoding the fusion constructs *CLCa-mEosFPthermo*, (murine) *mCav3-mEosFPthermo* or (zebrafish) *zfCav3-mEosFPthermo* using Lipofectamine 3000 (L300008, ThermoFisher Scientific). We used a high-copy number plasmid and the strong CMV promoter for transcription, ensuring that the endogenously expressed fractions of CLCa or Cav3 are negligible[1], so that the number of proteins in the structures can be determined. The medium was replaced by fresh medium after 5 h, and cells were imaged 24 h post transfection.

Immunolabeling of CCS on human cells. NCI-H1703 human lung carcinoma cells were cultured in RPMI 1640 medium (11835030, ThermoFisher Scientific) supplemented with 10% FBS. Cells were seeded on pre-cleaned round coverslips in 6-well plates and maintained at 37 °C and 5% CO_2 until they reached 50% confluency. NCI-H1703 cells were fixed with 4% paraformaldehyde in phosphate buffered saline (PBS) solution for 10 min. After washing twice with PBS (5 min each), cells were permeabilized with 0.5% Triton X-100 in PBS for 10 min. The sample was washed again twice with PBS and then with 5% bovine serum albumin (BSA) in PBS for 1 h to suppress unspecific binding. Then, the sample was incubated with 5 – 15 µg ml^{-1} Alexa647 labeled primary antibody against the CLCa chain (mouse monoclonal CLCa antibody, SPM174, Novus Biologicals) in BSA blocking buffer (5% BSA in PBS) at 37 °C for 2 h. Afterwards, the sample was washed with PBS three times in succession and imaged in dSTORM imaging buffer[2], containing 50 mM Tris (pH 8), 10 mM NaCl, 0.6 mg ml^{-1} glucose oxidase (G2133-250KU, Sigma-Aldrich), 33.8 µg ml^{-1} catalase (C40-100MG, Sigma-Aldrich), 10% (w/v) glucose and 1% (v/v) β-mercaptoethanol (Sigma-Aldrich).

Immobilization of mEosFP*thermo* on coverslips. Red fluorescent beads (FluoSpheres carboxylate-modified microspheres, diameter 20 nm, excitation 580 nm, emission 605 nm, ThermoFisher Scientific) were deposited on pre-cleaned coverslips by spin coating. Next, the coverslips were incubated with a 9:1 mixture of BSA and biotinylated BSA (both Sigma-Aldrich) with a total BSA concentration of 0.1 mg/ml for 5 min at room temperature. After washing with MilliQ water, the coverslips were incubated with NeutrAvidin (0.1 mg/ml, ThermoFisher Scientific) for 5 min at room temperature and washed again. Finally, the coverslips were exposed to biotinylated mEosFP*thermo* solution (180 pM in PBS) for 30 min at room temperature; unbound protein was removed by thorough washing with PBS.

Microscope and imaging procedures. Widefield microscopy and SMLM data were collected on a home-built TIRF microscope built around an Axio Observer Z1 body (Zeiss)[3]. The green and photoconverted red forms of mEosFP*thermo* were excited with a 473-nm laser (Gem 473, Laser Quantum) and a 561-nm laser (Gem 561, Laser Quantum), respectively. A 405-nm laser (Stradus 405-250, Vortran Laser Technology) was used for green-to-red photoconversion. The CLCa antibody-Alexa647 conjugate was imaged with 639-nm laser excitation (MRL-FN-639-500, Ultralasers). The laser beams were combined with dichroic mirrors and passed through an acousto-optical tunable filter (AOTF, model AOTFnC-400.650, A-A Opto-Electronic) for adjustment of the irradiation power. A custom-built 10× beam expander ensured uniform irradiation of a suitable region of interest (ca. 70 × 70 μm^2). The laser beam was focused on the back aperture of the objective (alpha Plan-Apochromat 63x/1.46 Oil Corr M27, Zeiss), and TIRF excitation was achieved by displacing the focus on the back aperture from the optical axis. The fluorescence emission was detected with a cooled (–90 °C) EMCCD camera (iXon Ultra 897, Andor).

Laser powers have to be carefully adjusted to obtain, on the one hand, a suitable signal level and SBR for SMLM and, on the other hand, minimal adverse effects of laser irradiation on cluster and hotspot lifetimes. Increasing the 561-nm power shortens the emission period of a photoactivated fluorophore, which may lead to fluorophore localization in a single frame rather than several consecutive ones. The reduced number of localization events in a cluster makes small, short-lived clusters disappear in the background, so the lifetime distribution apparently shifts to longer lifetimes (Fig. S8a). In addition, rapid photoactivation by 405-nm laser irradiation can deplete the pool of mEosFP fluorophores before the structure itself disappears. In the range of 405-nm laser powers available in our setup, we observed only a minor effect on the lifetime distributions (Fig. S8b). In the light of these control experiments, we kept the 561-nm excitation laser power below 0.07 kW cm^{-2} and the 405-nm photoactivation laser power in the range 0.015 – 0.028 W cm^{-2}.

Our image sequences were acquired with 10,000 frames (5-min measurement) and 60,000 frames (30-min measurement), with 30 ms dwell time each. From the images, we extracted the locations of all fluorophores using a-livePALM software[4] and assigned them to clusters. To cover the full temporal evolution of clusters, clusters appearing in the first 10 s and those still present in the last 10 s of the image sequence were discarded. For each construct, 5-min image sequences were collected on three different days, the numbers of imaged cells were 6, 7, 6 for CCS, 14, 15, 16 for mCav3 CAVSs and 18, 8, 12 for zfCav3 CAVSs. 30-min image sequences were taken (for hotspot lifetime analysis) on two days each on altogether 9 (CCS), 6 (mCav3 CAVSs) and 6 (zfCav3 CAVSs) cells.

Validation of LOF-DBSCAN and comparison to DBSCAN with synthetic data sets. After optimizing the input parameter sets for both algorithms (Fig. S2, Table S3), we evaluated the performance using data sets with homogeneous and heterogeneous background levels (Fig. S3). LOF-DBSCAN was much more reliable in the presence of heterogeneous background; its weak sensitivity to input parameters (Fig. S4) ensures minimal user bias. We further optimized these parameters with synthetic image sequences with an initially high but continuously decreasing SBR, which emulates the photobleaching effect of experimental sequences (Fig. S5). LOF-DBSCAN clearly outperformed DBSCAN on data sets with low SBR.

Corrections to fluorophore numbers in a cluster. Our SMLM analysis assigns localization events of individual fluorophores to clusters. The number of active emitters in a cluster, which results from assigning localizations appearing at the same positions in contiguous images to a particular fluorophore, is not equal to the real number of proteins for multiple technical reasons. (1) Endogenous expression of membrane coat proteins generates unlabeled proteins that we cannot detect. However, overexpression of our fluorescent fusion constructs ensures that this effect is negligible[5]. (2) Release of photobleached proteins from coat structures and recruitment of fluorescent ones from the cytoplasm during accumulation of a cluster can artificially increase the number of observed proteins. However, exchange of CLCa molecules between CCS and the cytoplasm was reported to be slow against the cluster lifetime[6]. This presumably holds true for Cav3 proteins in CAVSs as well, considering that they are integral membrane proteins well embedded in the plasma membrane. (3) Only a fraction of all expressed FPs convert to the red species upon photoactivation, which causes serious undercounting of proteins. For the EosFP variant mEos2, a photoactivation efficiency of 0.61 ± 0.02 has been reported[7]. Given the structural closeness of Eos2 and EosFP*thermo*, we have adopted this value for correction. (4) FPs are known to exhibit photoblinking, i.e., they can transiently switch to a long-lived dark state. Thus, mEosFP*thermo* (in the red-emitting state) may not turn dark permanently due to photobleaching but resume emission after an extended dark period. We cannot distinguish a previously observed, rekindled FP from a newly activated one and, therefore, this process causes

overcounting of FP molecules. A quantitative analysis of blinking of surface-immobilized molecules under comparable light irradiation yields an average of $2.0^{+1.2}_{-0.7}$ blinking events (errors indicate 95% confidence limits) per red-converted mEosFP*thermo* fluorophore (Fig. S12, Supplementary Text), in agreement with previous data on closely related FPs[8]. Accordingly, in this work, the raw molecule numbers have been scaled by a factor of 1.22 to account for blinking and incomplete photoactivation of mEosFP*thermo*.

SPT. CLCa, mCAV3 and zfCav3 fusion constructs with a carboxyterminally eGFP or mGarnet2[9] tag were excited by 473 or 561 nm laser light (2.4 W cm^{-2}, measured at the sample plane in wide-field mode) in TIRF mode. For each of the three FP fusions, independent measurements were performed on three different days. Three images (dwell time 100 ms, no lag time) were taken every 1.5 s for 5 min and were boxcar-averaged to increase the SBR before analysis with the cmeAnalysis package[5] to extract lifetimes. Lifetime histograms were calculated for each measurement day and scaled (by area) to the SMLM-derived probability density functions (PDFs).

Statistical analysis. For significance analysis of two independent data sets, we employed two-sample *t*-tests with unequal sample sizes and equal variances with null hypothesis at the 5 % significance level. Results are summarized in Table S4.

2. Supplementary Text

LOF-DBSCAN clustering algorithm

Step 1 – Identification of border localizations by LOF

For an object (localization event) *p* in the data set, the $k_{\text{distance}}(p)$ is defined as the distance from object *p* to the *k*-th nearest neighbor. Furthermore, the k_{distance} neighborhood, $N_k(p)$, of object *p* is defined as the set of objects, *q*, with distance from object *p*, $d_{pq} \leq k_{\text{distance}}(p)$.

The reachability distance of an object *p* with respect to another object *q* is defined as

$$reach\text{-}dist(p,q) = \max\{k_{distance}(p), d_{pq}\}. \quad (1)$$

The local reachability density of *p* is the inverse average of $reach\text{-}dist(q,p)$ within $N_k(p)$,

$$LRD_k(p) = \left(\frac{\sum_{q \in N_k(p)} reach\text{-}dist_k(p,q)}{|N_k(p)|}\right)^{-1}. \quad (2)$$

Finally, $LRD_k(p)$ is compared to the $LRD_k(q)$ values within $N_k(p)$. To this end, the local outlier factor, *LOF*, of object *p* is calculated as

$$LOF_k(p) = \frac{\sum_{q \in N_k(p)} \frac{LRD_k(q)}{LRD_k(p)}}{|N_k(p)|}. \quad (3)$$

Therefore, in the LOF algorithm, each object is scored with a *LOF* value, signaling a density change for objects at a cluster border ($LOF \approx 1$) or a constant density for objects inside a cluster or background region ($LOF \gg 1$). The *LOF* value served as a threshold (*LOF* value was set to 1.1 for cell data) and objects at a cluster border were removed from the data set.

Step 2 – Separation of cluster and background events

Cluster and background events can be distinguished on the basis of their *LRD* values (Eq. 2 above), which depend on the density of events in the images, however. Therefore, an *LRD* threshold separating clusters from background needs to be introduced that automatically adjusts to varying densities of events. To this end, we generated synthetic background images by randomly placing events onto a field of a given size. These simulations were performed 50 times under variation of the number of localizations within the density range found in the experimental data. We analyzed the *LRD* values in each simulated background image to determine the largest *LRD*, LRD_{max}, occurring in the image. The entire procedure was repeated three times to assess random fluctuations and to compute LRD_{max} averages. The mean LRD_{max} as a function of the number of localizations in a field of a given area is well described by a simple power law (Fig. S1c, Fig. S2b). In the LOF-DBSCAN program, LRD_{max} values

from the best-fit curve to the simulated data serve as thresholds for the analysis of real images with the corresponding density of localizations.

Step 3 – Cluster identification

DBSCAN[10] is a popular clustering algorithm that classifies localization events as cluster core, cluster border or background events. It uses two global parameters, radius "*eps*" and minimum number of points within the *eps* neighborhood – "*minPts*". For every object, the algorithm checks if there are *minPts* objects within the *eps* distance and identifies dense regions based on this criterion. We used DBSCAN to assign localization events to individual clusters in the background-filtered images.

Step 4 – Cluster expansion

Since border localizations were removed by LOF, these have to be reassociated with their respective clusters by cluster expansion. To this end, we examined each individual cluster in the raw data set and used features of DSets-DBSCAN[11] to precisely determine the *eps* radius for each cluster. We calculated 4^{th}-nearest distances, d_i, of each localization within each cluster. Then, the *eps* radius for each cluster was set to mean(d_i) + *expanding factor* × SD(d_i). *The expanding factor* was chosen as 1 for all data sets and the clusters were expanded with the locally determined *eps* radii and *minPts* = 4 by DBSCAN.

Validation

The F_1 score[12] was used for testing the clustering accuracy with LOF-DBSCAN, which considers both precision (ratio between the numbers of true positive events and the sum of true and false positive events) and recall (ratio between the numbers of true positive events and the sum of true positive and false negative events). Defined as the harmonic mean of precision and recall, the highest F_1 score is one.

$$F_1 = \frac{2}{recall^{-1} + precision^{-1}}. \quad (4)$$

Spherical clusters with different densities and radii were simulated and the performances of DBSCAN and LOF-DBSCAN were compared using F_1 scoring. With DBSCAN, different combinations of *eps* and *minPts* were applied to identify the parameter set with the highest F_1 score. LOF-DBSCAN has five parameters, *k* and *LOF threshold* for cluster extraction, *eps* and *minPts* for cluster identification, and *expanding factor* for the final expanding step. As clusters are spatially well separated, DBSCAN shows a good performance over a wide parameter range; therefore, optimization of the parameters *eps* and *minPts* for cluster identification is not necessary. For dense data set, a higher *expanding factor* leads to overexpanding of the clusters. For a safe comparison of other parameters over sparse and dense

data sets, the *expanding factor* was set to 1. Thus, only *k* and *LOF threshold* were optimized for LOF-DBSCAN with the F_1 scoring method.

Applying LOF-DBSCAN to dynamic data

All clusters that spatially overlap in the entire time of interest are first merged. The corresponding cumulative number of localizations is plotted as a time trace and a positive slope in a certain region of the trace indicates the presence of a cluster. Slope changes, which define start and end points of cluster formation, were identified by the MATLAB function 'findchangepts'. Change point detection is illustrated in Fig. S7, where ten intervals of cluster activity are identified from these change points.

Cluster formation is not always a steady process, but may show phases with different rates of protein accumulation. Therefore, a change point of the slope can also be found inside a cluster, so that adjacent intervals have to be merged. To correctly identify intervals without clustering activity, the slopes were first calculated for each interval and intervals with slopes < 0.05 localizations per frame were considered as gaps separating successive clusters (Fig. S7b,c).

Determination of cluster properties

Lifetime

Cluster lifetime is calculated as the time from the first localization to the last localization within a given cluster.

Diameter

From the SMLM images, apparent cluster diameters are determined by fitting two-dimensional Gaussian model functions to the clusters to extract the width parameters, σ_x and σ_y , in the *x* and *y* directions, respectively. The apparent width, $\sigma_{app} = \sqrt{\sigma_x^2 + \sigma_y^2}$, includes an additional broadening due to the localization uncertainty, which needs to be removed to obtain the real width. The localization precision of an individual event[13], $\sigma_{prec} \approx \sqrt{s^2/N + a^2/(12N)}$, scales with the inverse square root of the number of detected photons, $N^{-1/2}$. It further depends on the standard deviation of the point spread function, *s*, and the camera pixel size, *a*. For an entire cluster, we calculate the average over all contributing localization events, $\langle\sigma_{prec}\rangle$. Taking this broadening as Gaussian distributed, we obtain the real width parameter as $\sigma_{real} = \sqrt{\sigma_{app}^2 - \langle\sigma_{prec}\rangle^2}$. Then, we quote the diameter of membrane coat structures as the full width at half maximum, $FWHM = 2\sqrt{(2\ln 2)}\sigma_{real}$.

The intrinsic dynamics of these structures poses an additional complication, as clusters may change size and move in the image frame during the time of data acquisition. Therefore, we applied the "moving window binning" method[14] to each cluster (window size/step size: 50 frames/10 frames) and

fitted each window with a two-dimensional Gaussians. The reported width parameters σ_x and σ_y from last three windows were averaged for calculating σ_{app}. Therefore, the reported diameters correspond to the size at the end of their lifetimes.

Number of emitters

Two localizations are assigned to the same emitter if they appear in adjacent frames, and they are displaced from one another by a distance less than one camera pixel (corresponding to 109 nm at the sample plane for our microscope).

Single cluster growth dynamics

For each cluster, the cumulative curve of localizations versus time within each cluster was generated and abrupt changes in each cumulative curve were identified with a change point detection algorithm[15]. Then, slopes between consecutive change points were calculated. A growth phase was assigned by merging the intervals of three or more consecutive change points with slopes above a threshold of 3.5 localizations per second.

Photodynamics of mEosFPthermo

It is well known that fluorescent proteins (and other luminophores) show intermittency in their emission (blinking), indicating that they transiently enter dark states from where they rekindle until they finally fall victim to permanent photodestruction. As a result, there may be multiple, time-separated emitter events for a single fluorophore, which leads to overcounting of molecules. We have characterized the photodynamics of mEosFP*thermo* to correct for this effect.

Data collection

mEosFP*thermo* was sparsely immobilized on a pre-cleaned coverslip using biotin-NeutrAvidin linkage and imaged by TIRF microscopy (for experimental details, see Supplementary Methods), using the same experimental conditions as for CCS and CAVS imaging. Stage drift was compensated by fiducial markers (FluoSpheres carboxylate-modified microspheres, diameter 20 nm, excitation 580 nm, emission 605 nm, ThermoFisher Scientific). To examine and correct for chromatic aberration, we imaged multi-color beads (100 nm diameter) with 473 nm and 561 nm laser excitation, using the same filter sets as for imaging the green and red forms of mEosFP*thermo*. First, images of the green form of mEosFP*thermo* were acquired with low-power 473 nm laser excitation to minimize photobleaching. Then, the 405 nm laser was switched on to continuously photoconvert mEosFP*thermo* molecules to their red-emitting form while images (30 ms dwell time) were taken with 561 nm excitation. Data acquisition was stopped once essentially all mEosFP*thermo* proteins were photobleached.

Data analysis

SMLM images (in the red channel) were analyzed using a-live PALM software[4] to identify localization events. These data were further processed by DBSCAN for clustering spatially separated mEosFP*thermo* proteins. Only clusters overlapping with the (diffraction-limited) spots in the green image were used for further analysis. The photon time traces from the red channel signal were first thresholded (by the mean) to find transitions between the “off” and “on” states. Then the levels before and after such transitions was tested with a two-sample Student’s t-test to identify statistically significant changes.

To characterize blinking of mEosFP*thermo*, a four-state blinking model was applied (Fig. S12), according to which the number of emissive periods (blinkings) before photobleaching (N_{blink}), the fluorescence ON time, (t_{on}), before the fluorophore enters the dark state or permanently photobleaches, and the time the molecule resides in the dark state, t_{off}, can be modeled[16]. The occurrences of measured t_{on} and t_{off} periods can be described by exponential distributions,

$$P_{t_{on}}(t) = (k_d + k_b)e^{-(k_d+k_b)t}, \quad (5)$$

$$P_{t_{off}}(t) = k_r e^{-k_r t}. \quad (6)$$

Here, k_d and k_b are rate coefficients for transitions to transient and permanent (photobleached) dark states, respectively, and k_r is the rate coefficient of recovering from the transient dark state (Fig. S12). The probability of N_{blink} emissive phases occurring in an emission time trace is described by a negative binomial distribution,

$$P_{N_{mol}}(N_{blink}) = \binom{N_{blink} + N_{mol} - 1}{N_{blink}} (1-p)^{N_{blink}} p^{N_{mol}}, \quad (7)$$

where N_{mol} is the number of mEosFP*thermo* proteins colocalized in one spot. As NeutrAvidin has four binding sites for biotin and, thus, can bind more than one mEosFP*thermo* molecule, N_{mol} was allowed to vary in the analysis. The parameter $p = k_d/(k_d + k_b)$, denotes the probability that OFF switching results from entering a transient dark state. The probability of transition to the dark state p was then used to calculate the expectation value of N_{blink} for a single mEosFP*thermo* molecule according to

$$\overline{N_{blink}} = \frac{p}{1-p}. \quad (8)$$

Finally, the number of emitters in each cluster, $N_{emitters}$, was converted into the number of registered proteins,

$$N_{prot} = \frac{1}{C}\left(\frac{N_{emitters} - 1}{\overline{N_{blink}}}\right). \quad (9)$$

The parameter C represents the fraction (ca. 60%) of mEosFP*thermo* proteins detected in the red-emitting form[7].

3. **Supplementary Figures**

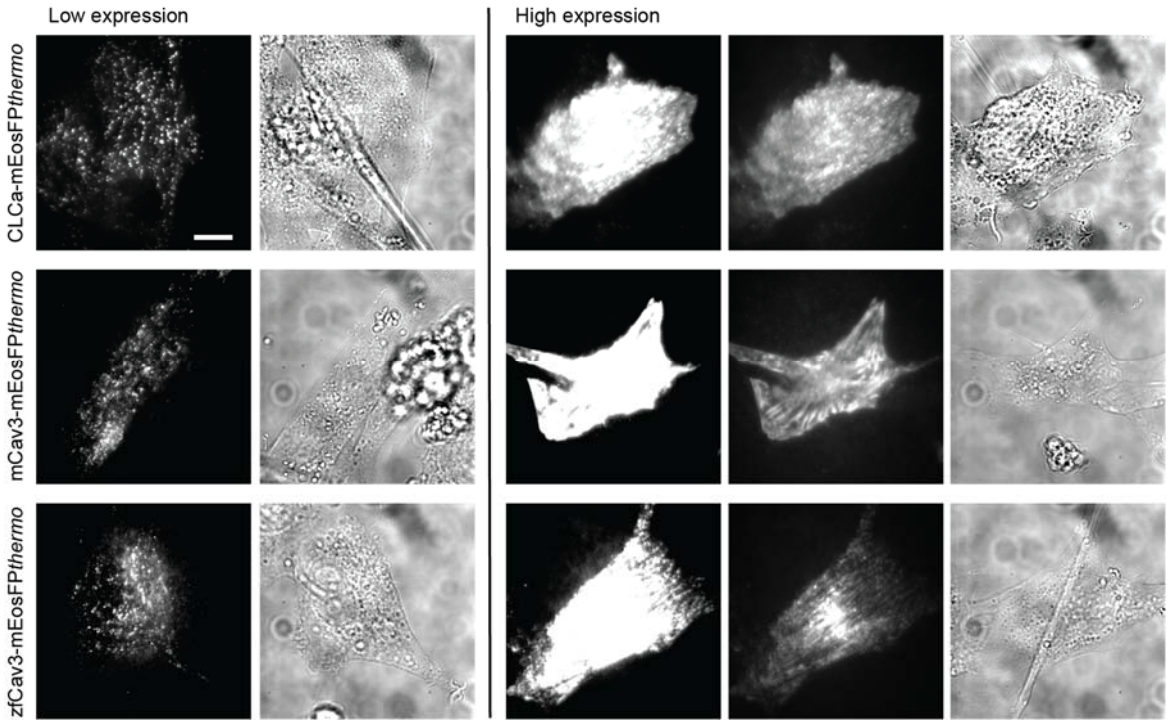

Fig. S1 Fluorescence and brightfield images of C2C12 cells expressing membrane coat proteins labeled with mEosFP*thermo*. The cells were transfected with 3 μg of plasmid DNA per 6 well plate; top row: *CLCa-mEosFPthermo;* middle row: (murine) *mCav3-mEosFPthermo*; bottom row, (zebrafish) *zfCav3-mEosFPthermo* constructs. The cells were visualized either by 473 nm laser excitation in TIRF mode (fluorescence) or by white-light illumination (brightfield). All images are shown as averages over 100 camera frames, each with 30-ms exposure. Column 1 (from the left): fluorescence; column 2: corresponding brightfield images, respectively, showing representative examples of cells with low expression. Note the punctate appearance of the labeled proteins in the fluorescence images and the proper cell morphology in brightfield mode. Columns 3 and 4: fluorescence; column 5: corresponding brightfield images, showing representative examples of cells with high expression. The images in column 3 are shown with the same brightness settings as column 1; the brightness was adjusted in column 4 to avoid overexposure. The characteristic punctate structures seen at low expression levels are not apparent in the fluorescence images, and the morphology is affected as well, especially for the *CLCa-mEosFPthermo* expressing cell. Selection of cells showing low expression avoids such overexpression artifacts. Scale bar, 10 μm.

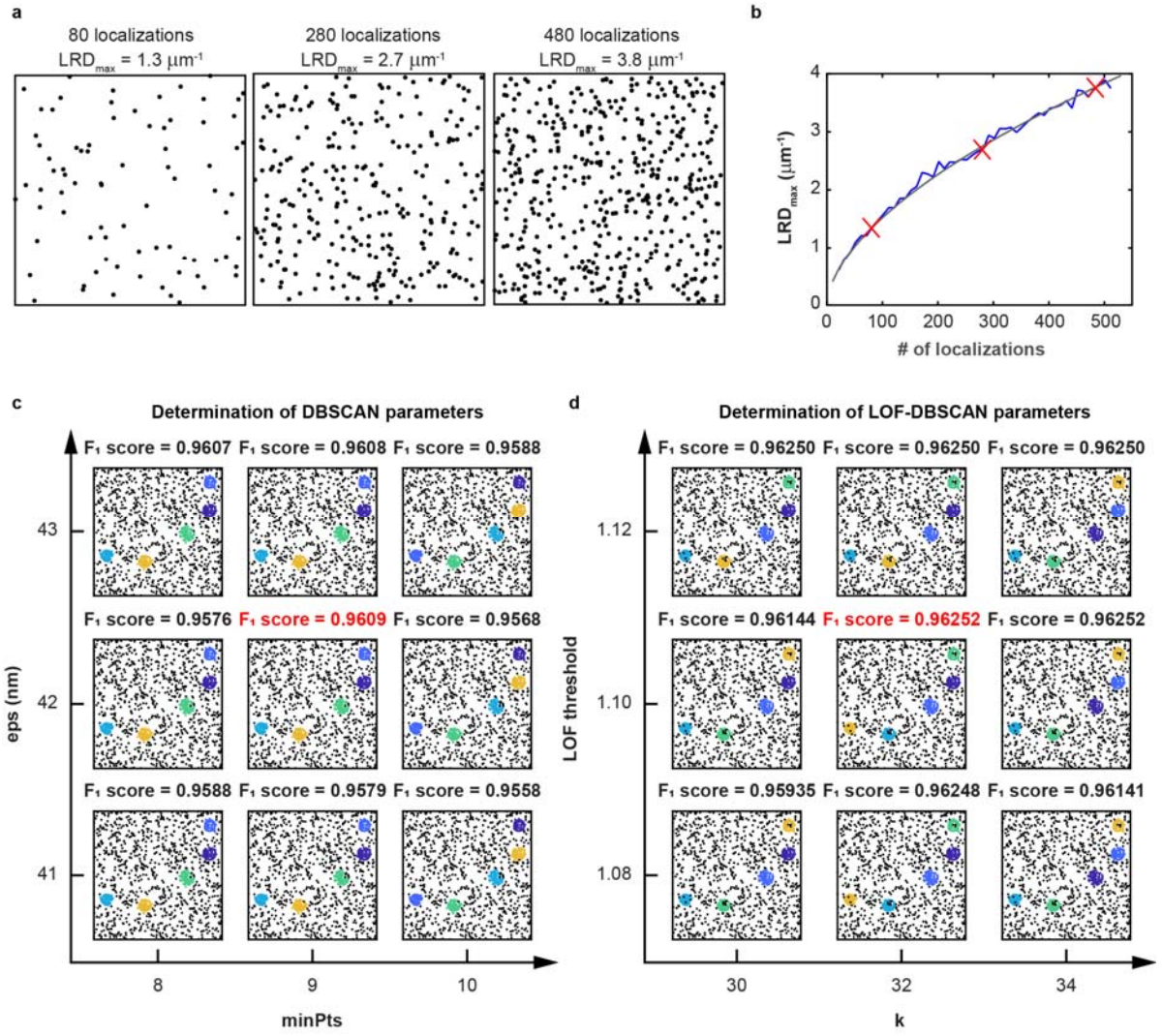

Fig. S2 Parameter determination for clustering algorithm. (**a**) Exemplary simulated background images (2.18 × 2.18 µm^2) at three selected localization densities; LRD$_{max}$ values were calculated with LOF parameter *k* = 30 (see Supplementary text). (**b**) Blue line: LRD$_{max}$, plotted against the number of localizations. Black line: Power law fit, $a \times (\#\ loc.)^b$, yielding a = 0. 108 µm^{-1} (95% confidence interval 0.096 µm^{-1}, 0.120 µm^{-1}) and b = 0.575 (95% confidence interval 0.556, 0.593). Red crosses: LRD$_{max}$ values corresponding to the images shown in **a**. Determination of optimal parameters for (**c**) DBSCAN and (**d**) LOF-DBSCAN by F_1 scoring[12]. The algorithms were applied to synthetic ground truth data sets (regions of interest shown: 2 × 2 µm^2), using combinations of *eps* and *minPts* for DBSCAN and *LOF threshold* and *k* for LOF-DBSCAN. Dots represent individual localizations; colored regions mark identified clusters (different colors for different clusters). Scores for the optimal parameter combinations are marked in red.

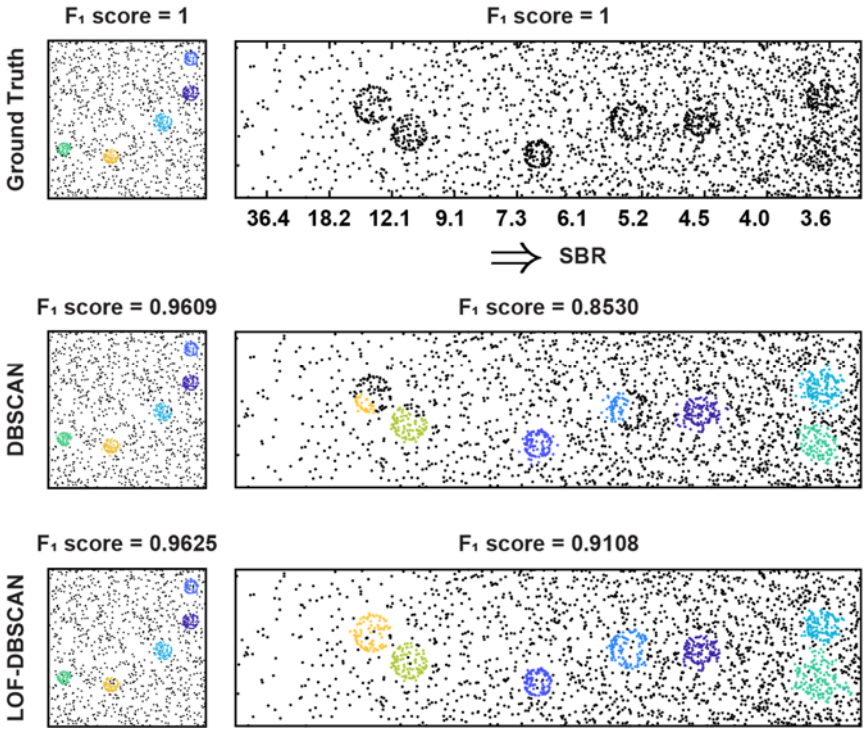

Fig. S3 Comparison of DBSCAN and LOF-DBSCAN using synthetic ground truth data sets with homogeneous (left, 2 × 2 μm^2) and inhomogeneous (right, 1 × 4 μm^2) background. Black dots correspond to the synthetic localizations and colored regions mark identified clusters (color-coding separates different clusters). The optimal parameters for both algorithms were taken from Fig. S2.

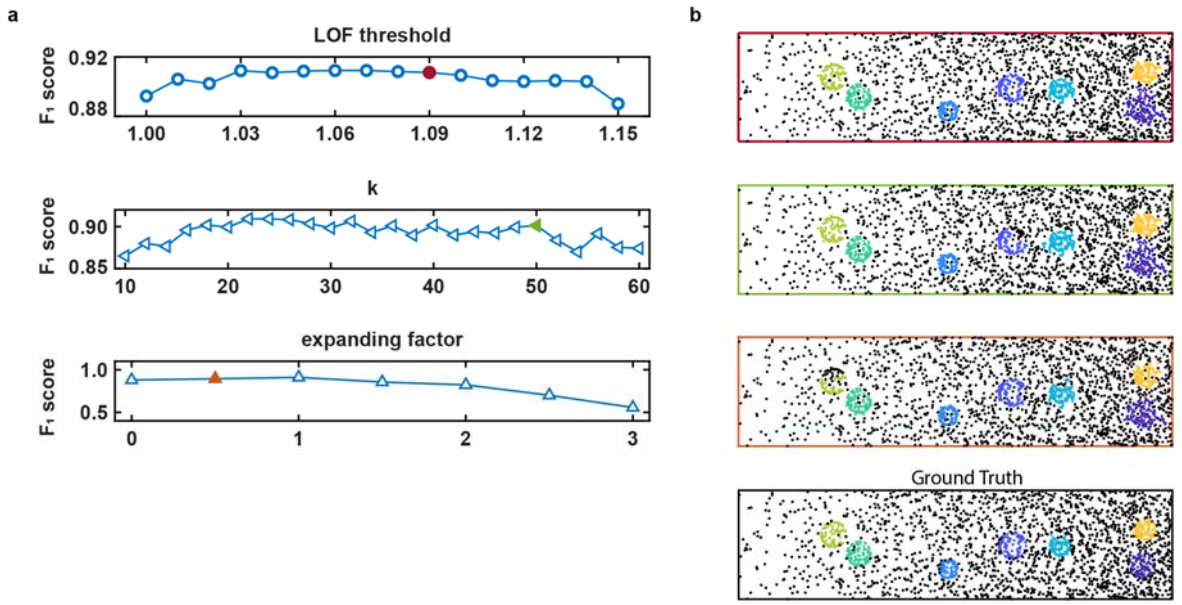

Fig. S4 Tuning range of LOF-DBSCAN parameters. (**a**) The optimal parameters determined by F_1 scoring for this data set were 1.06 for the *LOF threshold*, 25 for the number of nearest neighbors, *k*, and 1 for the *expanding factor*. Both the *LOF threshold* and *k* have a broad tuning range while maintaining good clustering performance. Solid data points indicate parameter values, which are suboptimal (measured by the F_1 score) and were used to demonstrate the robustness of LOF-DBSCAN. (**b**) LOF-DBSCAN applied to a synthetic data set with inhomogeneous background. In each row, the parameter scored on the left was set to the value indicated by the solid data point; the other two were set to their optimal values. Region of interest: 1×4 µm^2. Black dots correspond to the synthetic localizations and colored regions mark identified clusters (color-coding separates different clusters).

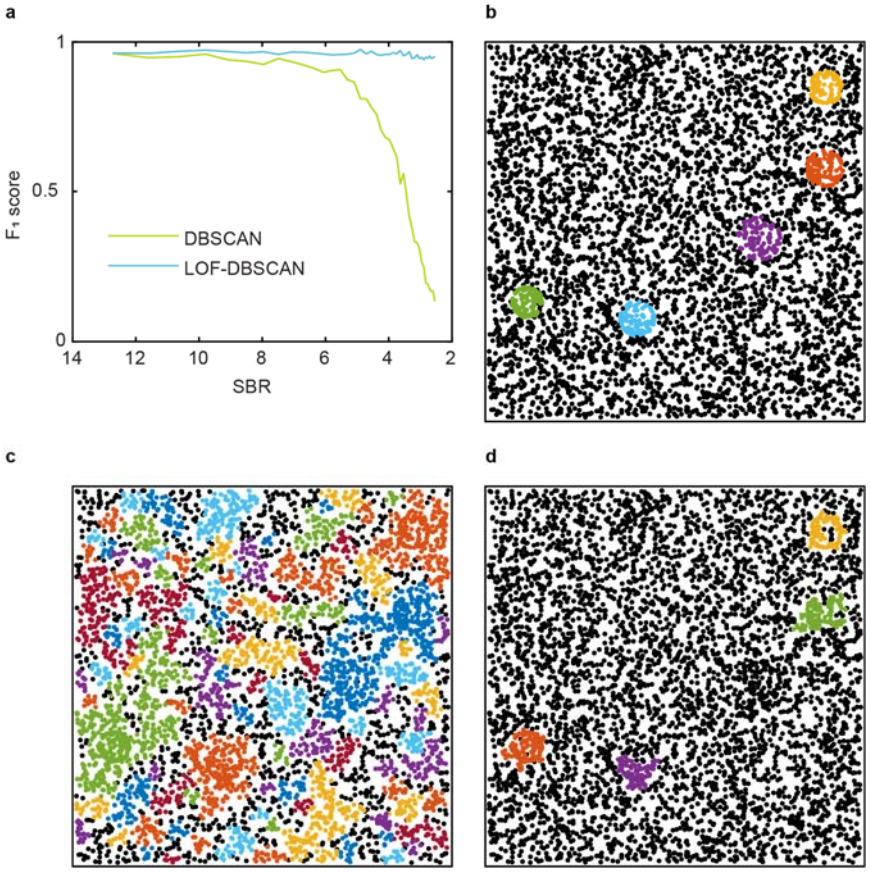

Fig. S5 Input parameter stability test for DBSCAN and LOF-DBSCAN. (**a**) F_1 scores of clustering results from DBSCAN, LOF-DBSCAN plotted as a function of (decreasing) SBR. (**b**) Ground truth data set with the lowest SBR of 2.5. Clustering results of (**c**) DBSCAN and (**d**) LOF-DBSCAN on the data set in panel **b**. In the simulated images, dots correspond to localizations; identified clusters are shown with colored dots.

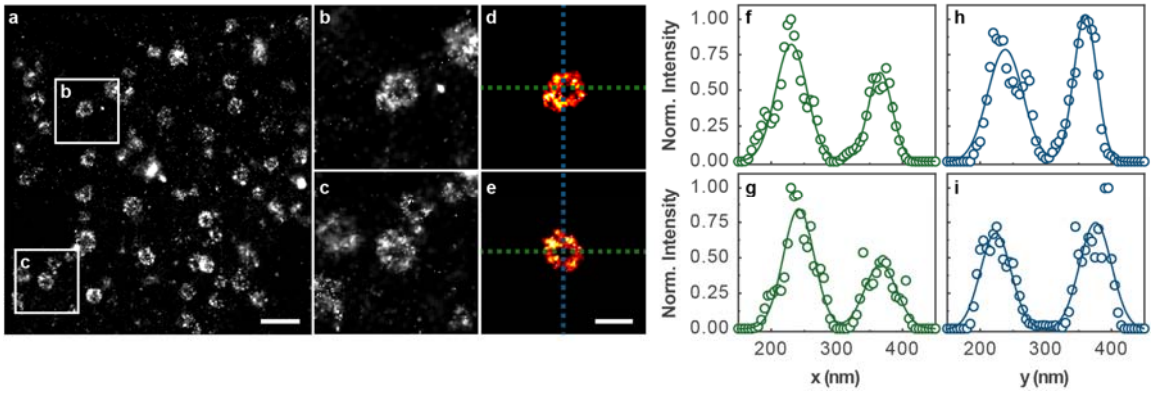

Fig. S6 Examples of CCP images of a fixed NCI-H1703 cell, immunolabeled with Alexa647-conjugated antibodies against CLCa (Supplementary Methods), segmented by LOF-DBSCAN. (**a**) SMLM image. (**b, c**) Expanded regions indicated by white squares in panel **a.** (**d, e**) Corresponding LOF-DBSCAN clustering results. Green and blue lines indicate where intensity profiles along the *x*- and *y*-directions were calculated, displayed in panels (**f-i**) in the corresponding colors. Scale bars, (**a**) 500 nm, (**b-e**) 200 nm.

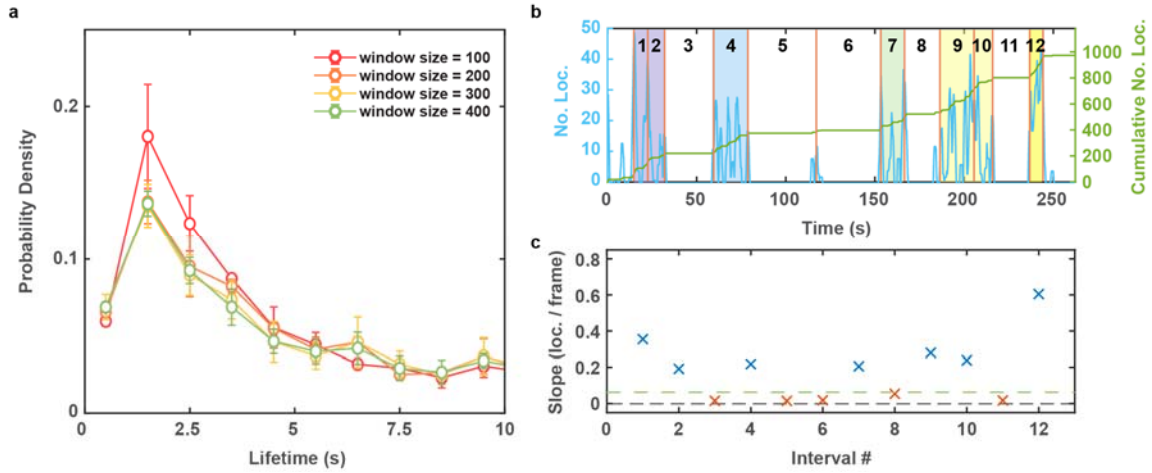

Fig. S7 TOI parameter selection and merging of localizations into clusters. (**a**) Effect of the number of frames combined in a TOI (window size) on the CCS cluster lifetime distribution. The image dwell time was 30 ms, the shift between subsequent TOIs was always 50 frames. At each lifetime interval, data are presented as mean (data point) and error bars (standard deviation, SD) of the cluster numbers from multiple cells. For comparison, all histograms were converted to probability densities by normalizing the areas under the curves to unity. As window sizes below 200 frames (6 s) resulted in an artificial shortening of cluster lifetimes due to an insufficient number of localizations, we used TOIs containing 300 frames (9 s) in our analysis. (**b**) The number of localizations versus time (blue) is converted into a cumulative curve (green line). A change-point detection algorithm finds abrupt changes in the cumulative curve (vertical orange lines). The slope of the cumulative curve in each interval between successive change points (here 12 intervals) was calculated and adjacent intervals with slopes < 0.05 localizations per frame (green dashed horizontal line) were merged into individual clusters. (**c**) Diagram of the slopes of the twelve intervals in **b**.

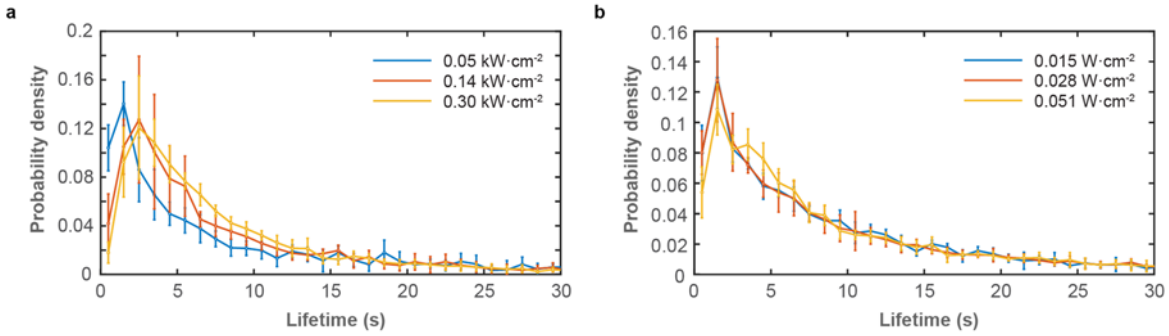

Fig. S8 Dependence of CCS cluster lifetime distributions on the laser intensity. Probability density functions are plotted as a function of cluster lifetime for three different powers of the (**a**) 561-nm fluorescence excitation laser and (**b**) 405-nm photoactivation laser. Powers (specified in the panels) were measured at the sample plane in widefield mode.

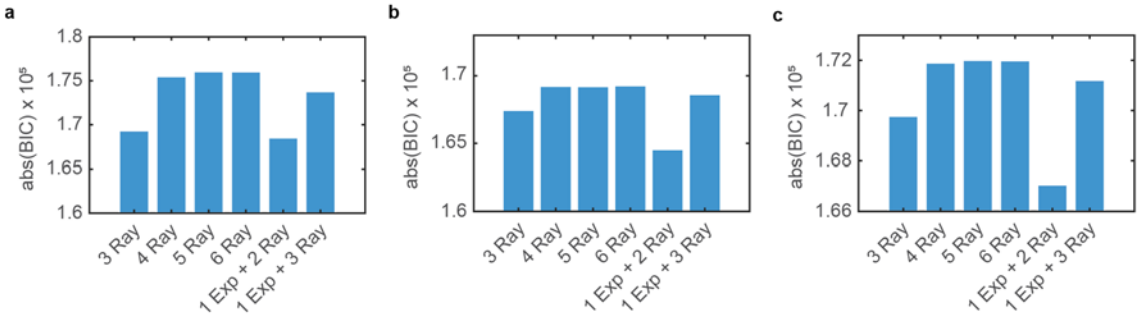

Fig. S9 Selection of the optimal model function (sum of multiple Rayleigh (plus exponential) distributions, as indicated) for lifetime histogram fitting by using the Bayesian information criterion (BIC). Absolute BIC values are plotted for (**a**) CCS (**b**) mCav3 CAVS and (**c**) zfCav3 CAVS data. Fits with three Rayleigh distributions (3 Ray) are inferior to 4, 5 and 6 Ray models, which work equally well. Including an exponential distribution gives again worse results. Thus, the analysis suggests taking 4 Ray as the simplest model that adequately describes the lifetime distributions.

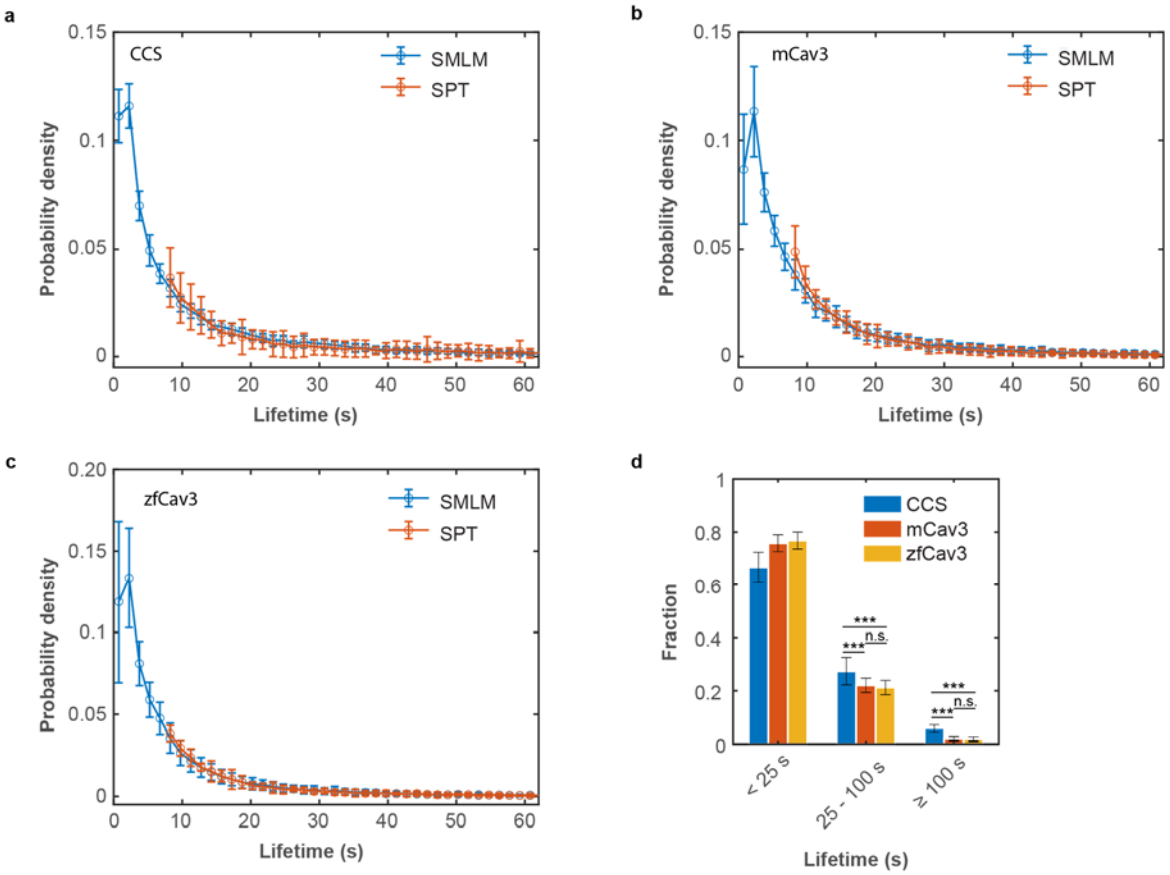

Fig. S10 Analysis of area-normalized cluster lifetime distributions (PDFs) from SMLM and SPT data, scaled to the SMLM data in the joint lifetime interval (7.5 – 100 s). (**a**) CCS, (**b**) mCav3 CAVS and (**c**) zfCav3 CAVS data. (**d**) Fractions of lifetime components in three different lifetime intervals, as determined by SPT. Data points correspond to averages; error bars represent SD values. Stars represent *P* values of a two-sample *t*-test, ***: $P < 0.001$, n.s.: not significant (for further details, see Supplementary Methods and Table S4).

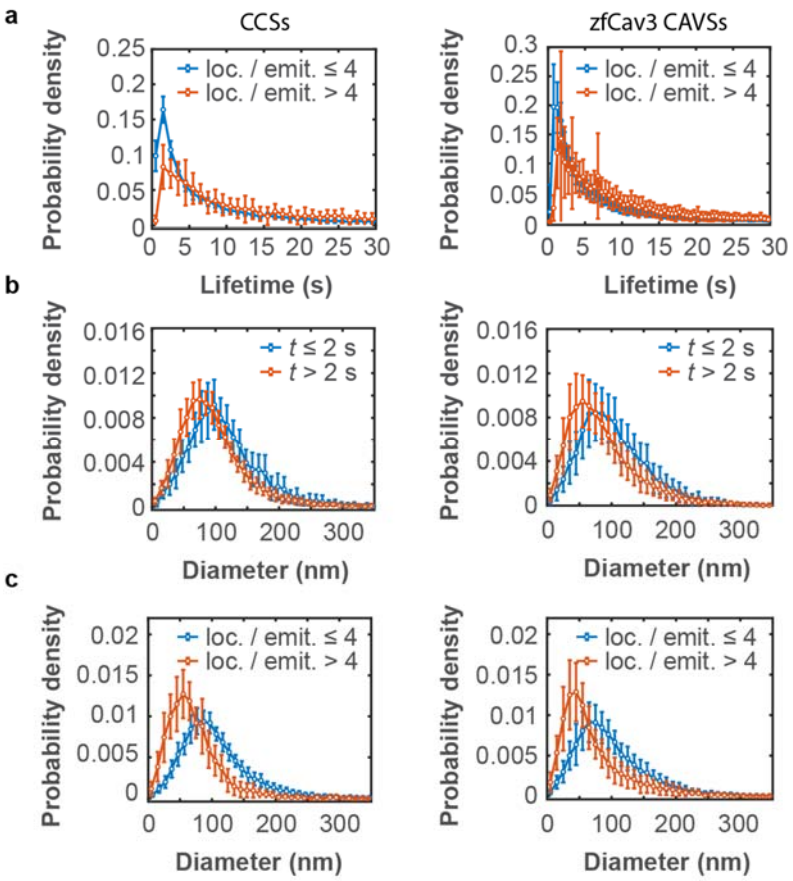

Fig. S11 PDFs of cluster lifetimes calculated with selected parameters for CCSs and CAVSs composed of zfCav3. (**a**) The populations with the shortest lifetimes are markedly greater for emitters with four or less localizations than with more than four localizations. Cluster diameters are greater for (**b**) $t \leq 2$ s and (**c**) four or less localizations of localizations per single emitter. These results consistently support the notion that clusters with very short lifetimes correspond to transiently appearing entities, including bigger structures (aggregates, vesicles) that are not associated with coat protein assembly.

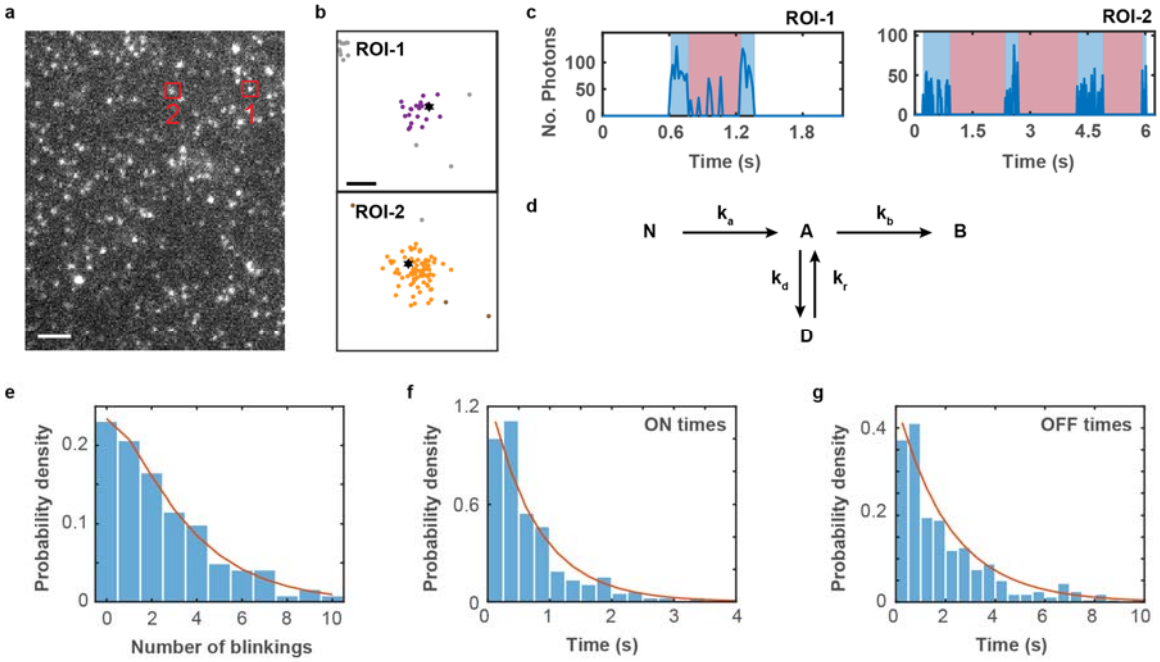

Fig. S12 Analysis of the photodynamics of mEosFP*thermo* immobilized on glass coverslips. For immobilization, coverslips were incubated with a 9:1 mixture of BSA and biotinylated BSA (both Sigma-Aldrich) with a total BSA concentration of 0.1 mg ml^{-1} for 5 min at room temperature. After washing with MilliQ water, the coverslips were incubated with NeutrAvidin (0.1 mg ml^{-1}, ThermoFisher Scientific) for 5 min at room temperature, washed again and exposed to biotinylated mEosFP*thermo* solution (180 pM in PBS) for 30 min at room temperature. Unbound protein was removed by thorough washing with PBS. (**a**) Conventional wide-field image of green mEosFP*thermo* proteins. Two representative regions of interest are marked by red frames. Scale bar, 2 µm. (**b**) Localizations of (red-converted) mEosFP*thermo* in the regions marked in (a). The black star represents the center of the protein spot in the green color channel (prior to photoconversion). Scale bar, 100 nm. (**c**) Representative photon time traces of selected regions; emissive (ON) and non-emissive (OFF) phases are shaded in blue and red, respectively. (**d**) Four-state kinetic model. N, A, D and B represent green, red, (transiently) dark and (permanently) bleached forms of mEosFP*thermo*, respectively. Arrows indicate transitions between the states with (in general intensity-dependent) rate coefficients *k* (transition probabilities). (**e**) PDF of the occurrence of blinking events of mEosFP*thermo*. The red curve shows a fit with a negative binomial distribution (see Supplementary Text) with two free parameters, $N_{mol} = 1.3 \pm 0.6$, the mean number of mEosFP*thermo* proteins colocalized in one spot, and $N_{blink} = 2.0^{+1.2}_{-0.7}$, the mean number of blinking events from an individual mEosFP*thermo* protein (errors indicate 95% confidence intervals). **(f** and **g**) PDFs of emission ON and OFF intervals, respectively, obtained from altogether 121 intensity time traces. According to the kinetic scheme in panel **d**, exponential fits (red lines) yield rate coefficients $k_d + k_b = 1.45^{+0.05}_{-0.06}\ s^{-1}$ (ON) and $k_r = 0.463 \pm 0.007\ s^{-1}$ (OFF). Errors indicate 95% confidence intervals.

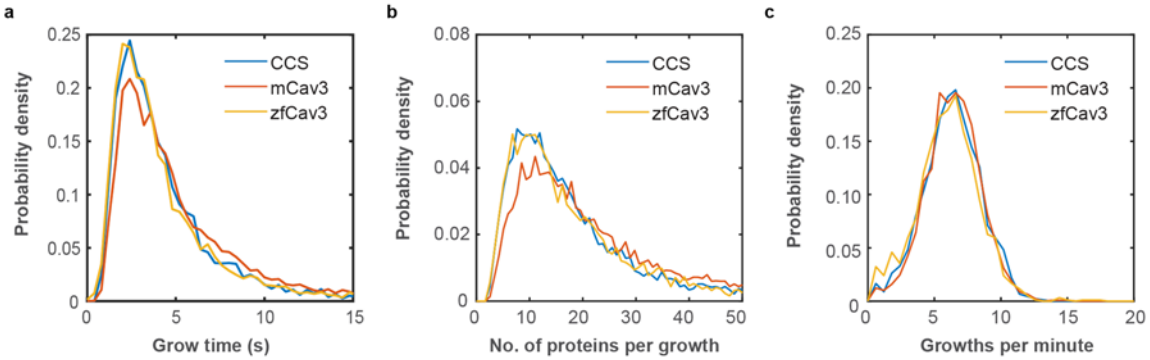

Fig. S13 Analysis of CCS and CAVS growth dynamics. (**a-c**) For individual CCS and CAVS clusters with lifetimes >50 s, PDFs are shown of (**a**) the duration of growth phases, (**b**) the number of incorporated protein molecules within each growth phase and (**c**) the number of growth phases per minute.

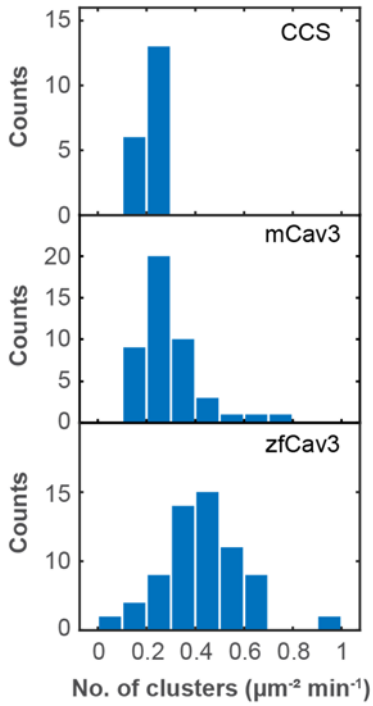

Fig. S14 Cluster density histograms of CCSs and CAVSs. For each cell, a square-shaped region of interest (ROI) within the cell was selected and clusters in that region were counted and normalized according to the ROI area and time. Each count in the histogram represents the cluster density of one cell. Averaging over the distributions yields mean cluster densities of 0.21 ± 0.04 μm^{-2} min^{-1} for CCSs, and 0.29 ± 0.12 μm^{-2} min^{-1} and 0.43 ± 0.17 μm^{-2} min^{-1} for mCav3 CAVSs and zfCav3 CAVSs, respectively.

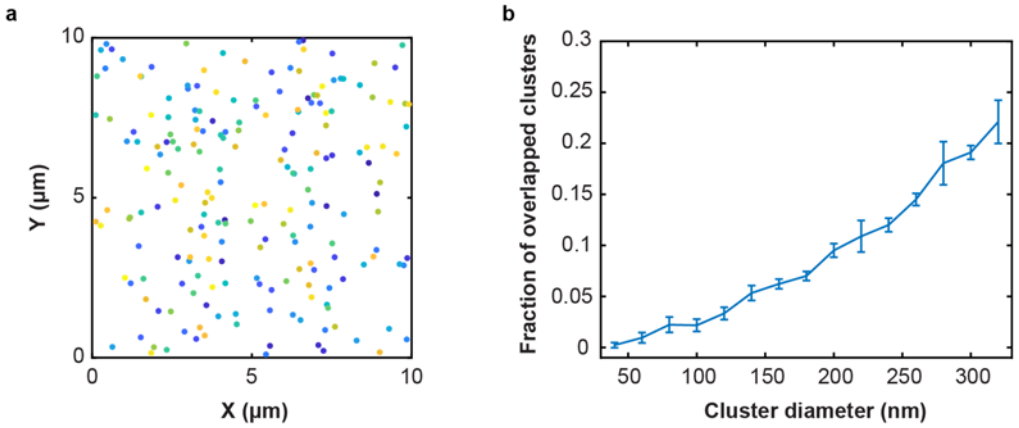

Fig. S15 Simulations of random distributions of clusters mimicking realistic experimental conditions. We took (for simplicity circular) clusters with diameters of 40 – 320 nm appearing at a rate of 0.3 μm^{-2} min^{-1}. Accordingly, altogether 600 clusters appeared on average in a field of view of 20 × 20 μm^2 in a 5-min SMLM image sequence, resulting in a similar cluster density as in the measurements (Fig. S14, Table S2). (**a**) Example of randomly placed clusters (colored dots) with 100-nm diameter. (**b**) Fraction of overlapped clusters as a function of cluster diameter. Data represent means (points) and SD (error bars) of three simulation cycles. The line connecting the data points is shown to guide the eye.

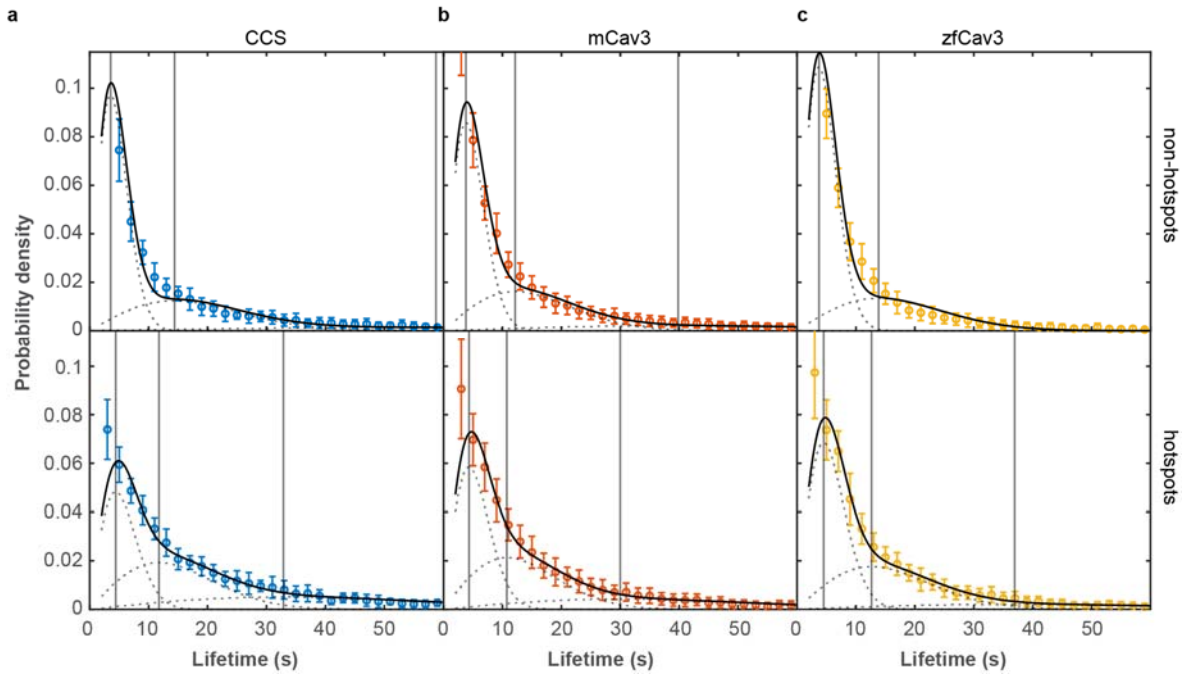

Fig. S16 Area-normalized cluster lifetime distributions (PDFs) of non-hotspot (top) and hotspot (bottom) (**a**) CCS, (**b**) mCav3 CAVS and (**c**) zfCav3 CAVS clusters. Only clusters with lifetimes $t > 2$ s were included in the analysis. In each lifetime interval ($\Delta t = 2$ s), cluster occurrences are plotted as means (data points) and SD (error bars) over multiple cells (19 cells for CCSs, 45 cells for mCav3 CAVSs and 38 cells for zfCav3 CAVSs). The data were fitted with sums of three Rayleigh distributions (black lines); individual subpopulations are shown as dotted curves. Vertical solid grey lines denote peak positions of the individual subpopulations.

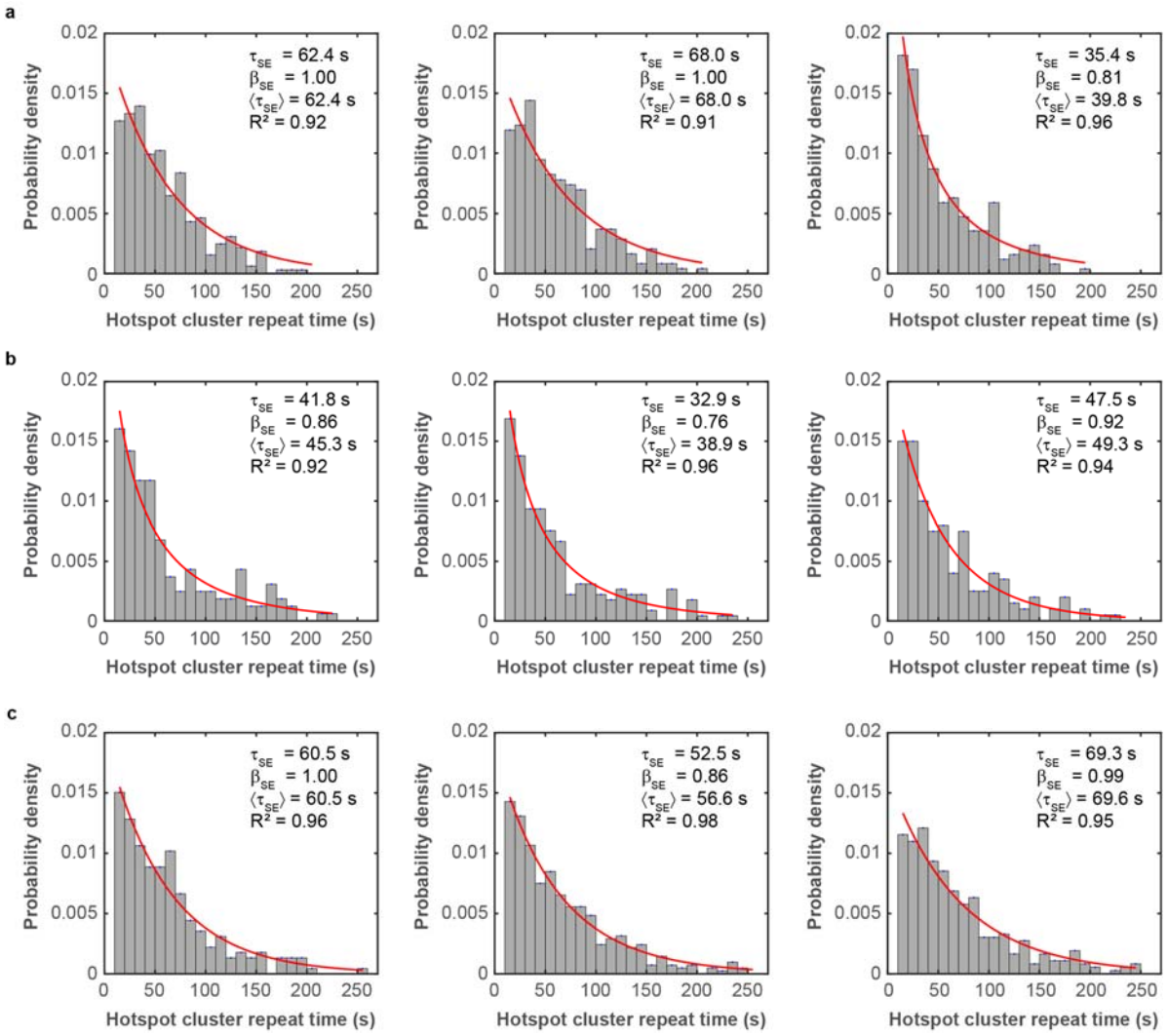

Fig. S17 Area-normalized histograms of hotspot cluster repeat times (grey) and fits with stretched exponentials (red) of (**a**) CCS, (**b**) mCav3 CAVS and (**c**) zfCav3 CAVS hotspots, with data shown for three representative cells each. For each panel, fit parameters of the stretched exponential, τ_{SE} and β, the average $\langle\tau_{SE}\rangle$ over the stretched exponential distribution, and the goodness of fit parameter (R^2) are given in the panels.

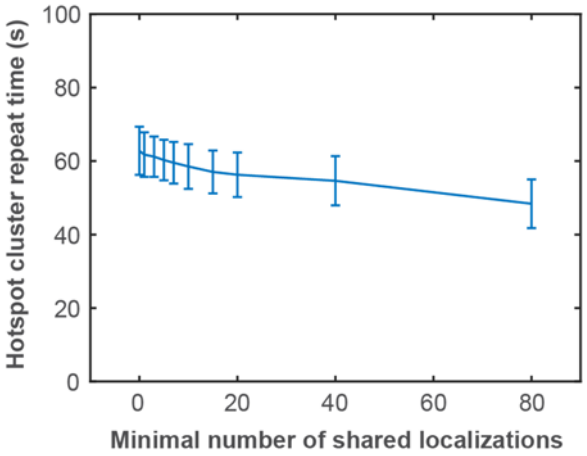

Fig. S18 Dependence of the hotspot cluster repeat time on the degree of spatial overlap (i.e., minimal number of shared localizations) demanded for sequentially occurring clusters. Data from the analysis of 5-min experiments on mCav3 CAVSs are shown as means (data points) and SD (error bars) over nine randomly selected cells (three cells each in three measurements on different days).

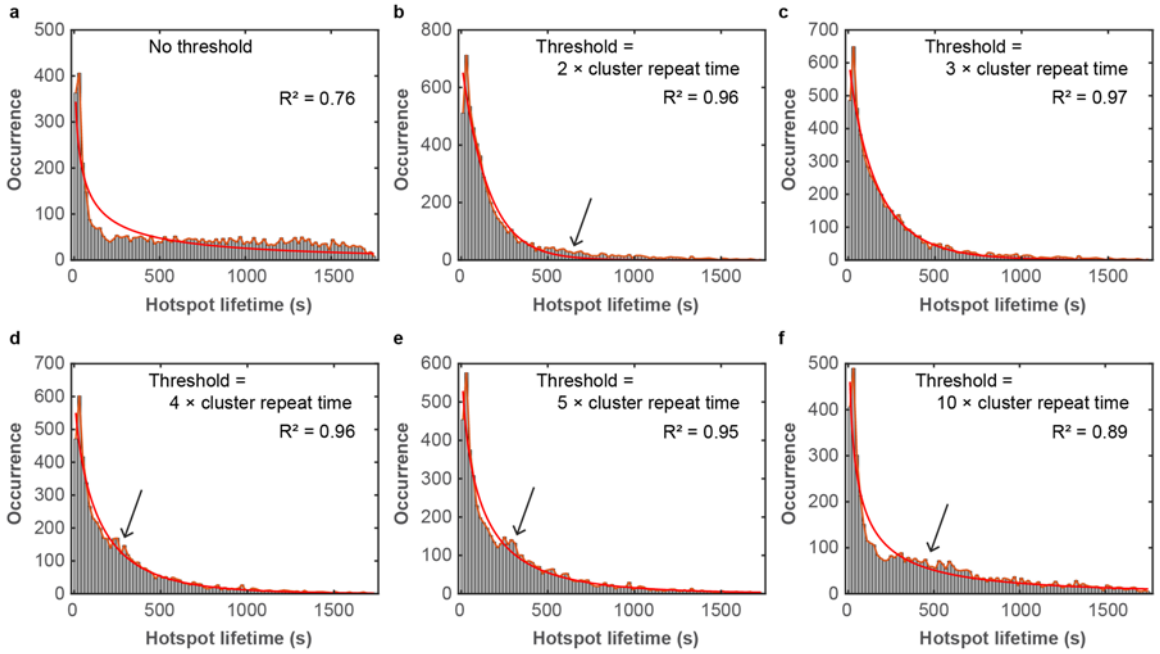

Fig. S19 Histograms of hotspot lifetimes determined from 30-min image sequences of mCav3 CAVSs, showing the total numbers of hotspots, binned in 20-s intervals, based on the observation of six cells. (**a**) Hotspot histogram based on the assignment of all clusters appearing over 30 min at the same spot. After a sharp drop at early times, the almost constant occurrence of longer lifetimes suggests that multiple, unrelated clusters appear at the same location over longer measurement times. We filter against such events by excluding cluster appearing with a time gap significantly larger than the usual cluster repeat times (~60 s, Table S5). To identify the optimal maximum time gap for assignment of a group of clusters to an individual hotspot, we varied the time gap from (**b-f**) 2 – 10-fold the cluster repeat time. The resulting histograms were fitted with stretched exponentials (red lines); the quality of the fit was assessed by the goodness-of-fit parameter R^2. Compared with the raw histogram in panel **a**, placing thresholds on the maximum time gap renders the distributions closer to monotonically decaying, as expected for random processes. Still, secondary peaks (black arrows) are present, which may arise if unrelated clusters or even hotspots are included in the lifetime calculation of a particular hotspot. These artifacts are minimized for a threshold of three times the average cluster repeat time (panel **c**). Therefore, this histogram was chosen for quantitative analysis of hotspot lifetimes (see Table S6 for parameters of all three membrane coat systems studied).

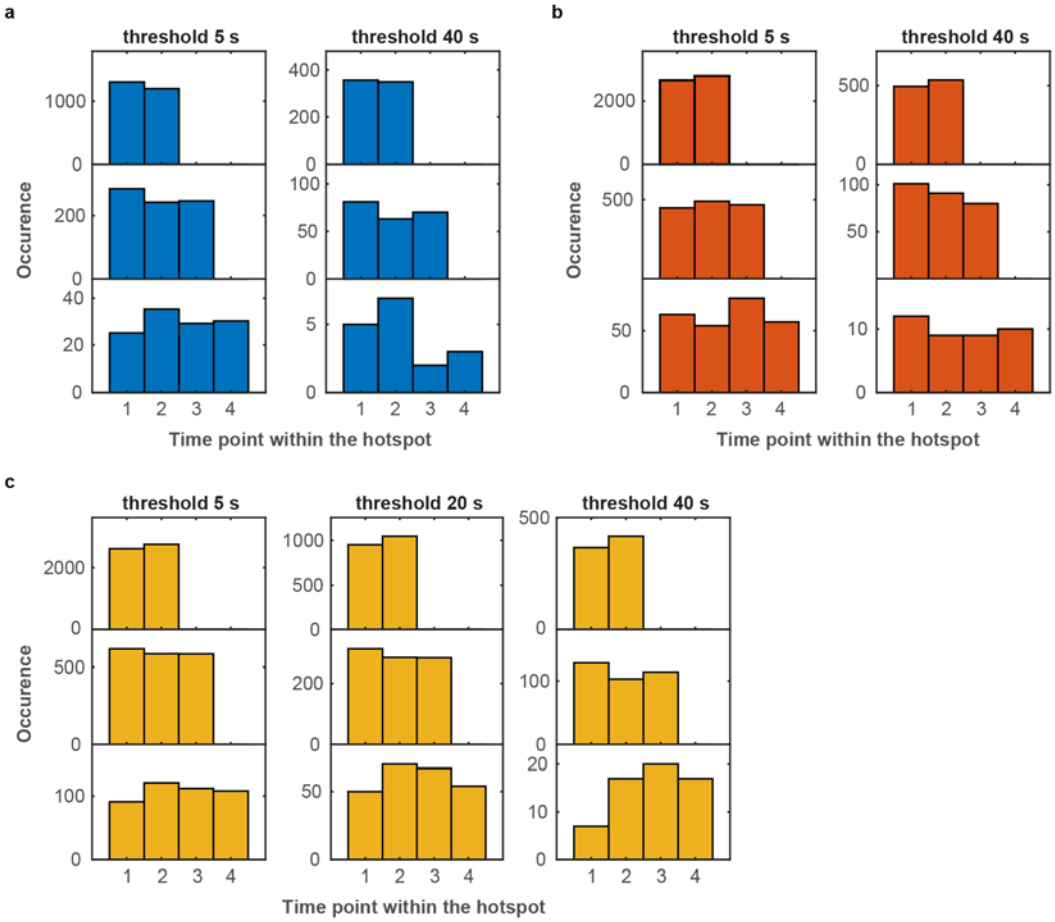

Fig. S20 Histograms of the position of the longest-lived clusters within the sequence of clusters belonging to (**a**) CCS, (**b**) mCav3 CAVS and (**c**) zf Cav3 CAVS hotspots. In the analysis based on the 5-min image sequences, the data were filtered to include longest-lived clusters within the hotspot with minimal lifetimes of 5 s, 20 s (data for CCSs and mCav3 CAVSs in the main text) and 40 s.

4. Supplementary Tables

Table S1 Compilation of plasmid constructs used in this study.

Plasmid name	Vector	Plasmid description	Reference
CLCa-mEosFP*thermo*	pEGFP	C-terminally tagged CLCa, CMV promoter	This study
mCav3-mEosFP*thermo*	pEYFP	C-terminally tagged mCav3, CMV promoter	This study
zfCav3-mEosFP*thermo*	pME	C-terminally tagged zfCav3, CMV promoter	This study
CLCa-eGFP	pEGFP	C-terminally tagged CLCa, CMV promoter	This study
mCav3-eGFP	pEYFP	C-terminally tagged mCav3, CMV promoter	This study
zfCav3-mGarnet2	pME	C-terminally tagged zfCav3, CMV promoter	This study

Table S2 CCS and CAVS cluster densities and diameters, averaged over the data set from 5-min image sequences. Determination of cluster diameters is described in Supplementary Text.

	Cluster density (μm^{-2} min^{-1})	Cluster diameter (nm)
CCS	0.21 ± 0.04	97 ± 10
mCav3	0.29 ± 0.12	83 ± 13
zfCav3	0.43 ± 0.17	87 ± 14

Errors represent SD values.

Table S3 Optimized parameter sets for DBSCAN and LOF-DBSCAN from the analysis of synthetic data with homogeneous/inhomogeneous background.

DBSCAN	**minPts**	**eps (nm)**	
Homogeneous background	9	42	
Inhomogeneous background	27	63	
LOF-DBSCAN	**k**	**LOF threshold**	**expanding factor**
Homogeneous background	32	1.1	1
Inhomogeneous background	25	1.06	1

Table S4 Parameters of the two-sample *t*-test with equal variances and unequal sample sizes.

Appearance	Tested samples		Sample size (# of cells)	*t* values	*P* values	Degrees of freedom
Fig. 3c	t < 25 s	CCS x mCav3	19, 45	-3.6	6×10^{-4}	62
		mCav3 x zfCav3	45, 38	-5.5	5×10^{-7}	81
		CCS x zfCav3	19, 38	-8.9	4×10^{-12}	55
	25 s ≤ t < 100 s	CCS x mCav3	19, 45	2.8	0.007	62
		mCav3 x zfCav3	45, 38	5.5	4×10^{-7}	81
		CCS x zfCav3	19, 38	7.9	1×10^{-10}	55
	t ≥ 300 s	CCS x mCav3	19, 45	7.1	2×10^{-9}	62
		mCav3 x zfCav3	45, 38	3.1	0.003	81
		CCS x zfCav3	19, 38	10.8	3×10^{-15}	55
Fig. S10d	t < 25 s	CCS x mCav3	12, 10	-8.2	7×10^{-8}	20
		mCav3 x zfCav3	10, 6	-0.7	0.49	14
		CCS x zfCav3	12, 6	-7.4	1×10^{-6}	16
	25 s ≤ t < 100 s	CCS x mCav3	12, 10	6.8	1×10^{-6}	20
		mCav3 x zfCav3	10, 6	0.68	0.5	14
		CCS x zfCav3	12, 6	6.1	1×10^{-5}	16
	t ≥ 300 s	CCS x mCav3	12, 10	8.8	2×10^{-8}	20
		mCav3 x zfCav3	10, 6	0.5	0.63	14
		CCS x zfCav3	12, 6	7.6	1×10^{-6}	16
Fig. 5b	1 cluster / area	CCS x mCav3	19, 45	-4.9	8×10^{-6}	62
		mCav3 x zfCav3	45, 38	-1.8	0.08	81
		CCS x zfCav3	19, 38	-5.3	2×10^{-6}	55
	2 clusters / area	CCS x mCav3	19, 45	4.1	1×10^{-4}	62
		mCav3 x zfCav3	45, 38	3.5	8×10^{-4}	81
		CCS x zfCav3	19, 38	6.6	2×10^{-8}	55
	3 clusters / area	CCS x mCav3	19, 45	4.6	2×10^{-5}	62
		mCav3 x zfCav3	45, 38	0.3	0.7	81
		CCS x zfCav3	19, 38	3.8	4×10^{-4}	55

Table S5 Quantification of hotspot cluster repeat times from 5-min SMLM image sequences; $\langle \tau_{HCR} \rangle$ values represent plain averages calculated from all measured cells. Additionally, single-cell distributions of hotspot cluster repeat times and minimal hotspot lifetimes were fitted with stretched-exponential model functions. Lifetime parameters, τ_{SE}, and stretching exponents, β, are averages over all cells in the ensemble. Notably, $\beta \approx 1$ (corresponding to a single exponential) within the error. Average lifetimes of the stretched exponential distribution, $\langle \tau_{SE} \rangle$, are also included.

Hotspot cluster repeat time	$\langle t_{HCR} \rangle$ (s)	$\boldsymbol{\tau_{SE}}$ (s)	$\boldsymbol{\beta}$	$\langle \boldsymbol{\tau_{SE}} \rangle$ (s)
CCSs	62 ± 4	63 ± 12	0.977 ± 0.060	64 ± 11
mCav3 CAVSs	60 ± 7	43 ± 18	0.832 ± 0.162	47 ± 16
zfCav3 CAVSs	65 ± 7	59 ± 16	0.928 ± 0.106	61 ± 14

Only parameters from fits with stretched exponentials with goodness-of-fit $R^2 > 0.8$ were included in the averaging. Errors correspond to SD.

Table S6 Quantification of hotspot lifetimes from 30-min SMLM image sequences by fitting stretched exponentials to hotspot lifetime distributions (Fig. 4e). Best-fit lifetime parameters, τ_{SE}, and stretching exponents, β, as well as average lifetimes of the stretched exponential distribution, $\langle\tau_{SE}\rangle$, are included.

Hotspot lifetime	$\boldsymbol{\tau_{SE}}$ $(\boldsymbol{s})$	$\boldsymbol{\beta}$	$\langle\boldsymbol{\tau_{SE}}\rangle$ $(\boldsymbol{s})$
CCSs	307 ± 53	1.000 ± 0.191	307 ± 53
mCav3 CAVSs	161 ± 23	0.858 ± 0.108	174 ± 25
zfCav3 CAVSs	185 ± 34	0.929 ± 0.167	191 ± 34

Errors correspond to the boundaries of the 95% confidence intervals.

5. Supplementary References

1 X. Wang, Z. Chen, M. Mettlen, J. Noh, S. L. Schmid and G. Danuser, *Elife*, 2020, **9**, 1–27.

2 G. T. Dempsey, J. C. Vaughan, K. H. Chen, M. Bates and X. Zhuang, *Nat. Methods*, 2011, **8**, 1027–1036.

3 Y. Li, L. Shang and G. U. Nienhaus, *Nanoscale*, 2016, **8**, 7423–7429.

4 Y. Li, Y. Ishitsuka, P. N. Hedde and G. U. Nienhaus, *ACS Nano*, 2013, **7**, 5207–5214.

5 F. Aguet, C. N. Antonescu, M. Mettlen, S. L. Schmid and G. Danuser, *Dev. Cell*, 2013, **26**, 279–291.

6 A. Hoffmann, P. N. Dannhauser, S. Groos, L. Hinrichsen, U. Curth and E. J. Ungewickell, *Traffic*, 2010, **11**, 1129–1140.

7 N. Durisic, L. Laparra-Cuervo, Á. Sandoval-Álvarez, J. S. Borbely and M. Lakadamyali, *Nat. Methods*, 2014, **11**, 156–162.

8 R. Richardson, C. L. Denis, C. Zhang, M. E. O. Nielsen, Y. C. Chiang, M. Kierkegaard, X. Wang, D. J. Lee, J. S. Andersen and G. Yao, *Mol. Genet. Genomics*, 2012, **287**, 711–730.

9 G. Matela, P. Gao, G. Guigas, A. F. Eckert, K. Nienhaus and G. Ulrich Nienhaus, *Chem. Commun. (Camb).*, 2017, **53**, 979–982.

10 M. Ester, H.-P. Kriegel, J. Sander and X. Xu, In *Proceedings of the Second International Conference on Knowledge Discovery and Data Mining*, 1996, pp. 226–231.

11 J. Hou, H. Gao and X. Li, *IEEE Trans. Image Process.*, 2016, **25**, 3182–3193.

12 B. Larsen and C. Aone, In *Proceedings of the Fifth International Conference on Knowledge Discovery and Data Mining*, New York, New York, USA, 1999, pp. 16–22.

13 R. E. Thompson, D. R. Larson and W. W. Webb, *Biophys. J.*, 2002, **82**, 2775–2783.

14 L. Zhou, M. Evangelinos, V. Wernet, A. F. Eckert, Y. Ishitsuka, R. Fischer, G. U. Nienhaus and N. Takeshita, *Sci. Adv.*, 2018, **4**, 1–10.

15 R. Killick, P. Fearnhead and I. A. Eckley, *J. Am. Stat. Assoc.*, 2012, **107**, 1590–1598.

16 S.-H. Lee, J. Y. Shin, A. Lee and C. Bustamante, *Proc. Natl. Acad. Sci. U. S. A.*, 2012, **109**, 17436–17441.